Nanoscale

PAPER

View Article Online
View Journal

Cite this: DOI: 10.1039/c4nr01645a

Monolithic NPG nanoparticles with large surface area, tunable plasmonics, and high-density internal hot-spots†

Fusheng Zhao,‡[a] Jianbo Zeng,‡[a] Md Masud Parvez Arnob,[a] Po Sun,[a] Ji Qi,[a] Pratik Motwani,[a] Mufaddal Gheewala,[a] Chien-Hung Li,[b] Andrew Paterson,[c] Uli Strych,[c] Balakrishnan Raja,[c] Richard C. Willson,[c] John C. Wolfe,[a] T. Randall Lee[b] and Wei-Chuan Shih*[a]

Received 26th March 2014
Accepted 7th May 2014

DOI: 10.1039/c4nr01645a

www.rsc.org/nanoscale

Plasmonic metal nanostructures have shown great potential in sensing, photovoltaics, imaging and biomedicine, principally due to the enhancement of local electric field by light-excited surface plasmons, *i.e.*, collective oscillation of conduction band electrons. Thin films of nanoporous gold have received a great deal of interest due to the unique 3-dimensional bicontinuous nanostructures with high specific surface area. However, in the form of semi-infinite thin films, nanoporous gold exhibits weak plasmonic extinction and little tunability in the plasmon resonance, because the pore size is much smaller than the wavelength of light. Here we show that by making nanoporous gold in the form of disks of sub-wavelength diameter and sub-100 nm thickness, these limitations can be overcome. Nanoporous gold disks not only possess large specific surface area but also high-density, internal plasmonic "hot-spots" with impressive electric field enhancement, which greatly promotes plasmon–matter interactions as evidenced by spectral shifts in the surface plasmon resonance. In addition, the plasmonic resonance of nanoporous gold disks can be easily tuned from 900 to 1850 nm by changing the disk diameter from 300 to 700 nm. Furthermore, nanoporous gold disks can be fabricated as either bound on a surface or as non-aggregating colloidal suspension with high stability.

Metal nanostructures exhibit collective oscillation of conduction band electrons excited by incident light.[1] The associated enhanced electric field near the surface of metal nanostructures, known as *surface plasmon resonance* (SPR) for propagating fields or *localized surface plasmon resonance* (LSPR) for non-propagating ones, has been well studied and is widely used in optical sensors,[2] photovoltaic devices,[3] waveguides,[4] imaging devices,[5] SHINERS,[6] and biomedicine.[7,8] Both SPR and LSPR strongly depend on the composition, shape and size of metal nanostructures, as well as the ambient environment.[9] Therefore, controlling their composition, shape and size is essential for potential applications.

Bulk nanoporous gold (NPG) as a nanostructured semi-infinite thin film material exhibits tunable pore and ligament sizes ranging from nanometers to microns.[10] It can be produced by either dealloying the less noble constituent of a gold alloy or by electrochemical corrosion. Its large specific surface area, crystalline alignment, and clean surface make NPG an attractive unsupported catalyst.[11,12] In addition to its catalytic activity, NPG also exhibits interesting optical properties, such as mixed states of localized/propagating surface plasmons because of the nanoscale ligaments and pore channels within the unique 3-dimensional bicontinuous porous nanostructures.[13–15] The plasmonic properties of NPG have been explored for molecular sensing using "as-dealloyed",[16] mechanically stamped,[17] or wrinkled films[18] as well as lithographically patterned monolithic NPG disks with a diameter smaller than the wavelength of natural light.[19,20] In "as-dealloyed" NPG thin films, the LSPR band centering around 600 nm has a limited tunability of about 50 nm, achieved by varying the pore size from 10 to 50 nm.[16] In mechanically stamped NPG thin films, the grating modulation provides a propagating SPR mode coupled with NPG's original LSPR band. However, the plasmonic landscape is dominated by the NPG LSPR. Furthermore, in thermally wrinkled NPG thin films, random, sparse plasmonic hot-spots form at gaps and

[a]*Department of Electrical and Computer Engineering, University of Houston, 4800 Calhoun Road, Houston, TX 77204-4005, USA. E-mail: wshih@uh.edu; Fax: +1-713-743-4444; Tel: +1-713-743-4454*

[b]*Department of Chemistry and the Texas Center for Superconductivity, University of Houston, Houston, TX 77204-5003, USA*

[c]*Department of Chemical and Biomolecular Engineering, University of Houston, Houston, TX 77204-5001, USA*

† Electronic supplementary information (ESI) available: Chemicals, materials, and characterization for the experimental section. IR, XPS, buoyant mass and extinction data for NPG disks. See DOI: 10.1039/c4nr01645a

‡ These authors contributed equally.

junctions due to structural deformation, and thus would not alter the average plasmonic behavior.

The enhanced electromagnetic fields of LSPR excited in the ligaments are considered to be a major contributor to surface-enhanced optical phenomena, such as surface-enhanced Raman scattering (SERS) and surface-enhanced fluorescence.[21] In previous work, lithographically patterned NPG disks demonstrated an excellent SERS activity, representing the first attempt to produce quasi-one-dimensional NPG nanostructures that drastically departed from semi-infinite NPG thin films.[19,20] NPG disks exhibit nanoporosity mimicking that of mesoporous silica; however, they are plasmonically active. The structural hierarchy of NPG disks differs from the existing plasmonic nanoparticles such as Au or Ag nanospheres, nanorods, nanoshells, and nanocages, which lack internal nanoporous structures.

In this work, we report the nanofabrication of uniform, monolithic NPG disks and in-depth studies of their plasmonic properties. We demonstrate that substrate-bound NPG disks can be released and harvested as colloidal nanoparticles, which differ drastically from the existing NPG materials, and can be viewed as a novel functional material. NPG disks feature a well-defined "exterior" disk shape of 300–700 nm diameter and 75 nm thickness, and an "interior" 3-dimensional porous network with pore sizes of ~13 nm. We show, for the first time, that NPG disks inherit LSPR features from both the nanoporous structures and the sub-wavelength disk shape. Coupling between these two LSPRs results in intriguing plasmonic properties. Nanoporous plasmonic disks not only possess large specific surface area but also high-density internal plasmonic "hot-spots" with impressive electric field enhancement, which greatly promotes plasmon–matter interactions as evidenced by the high LSPR sensitivity to the ambient environment.

Results and discussion

NPG disk fabrication

To fabricate NPG disks, we take advantage of both top-down lithographic patterning and bottom-up atomic dealloying, which together demonstrate great synergy in precisely tuning the plasmonic properties of nanoporous materials.[17,20] As shown in Scheme 1, a film of gold and silver alloy approximately 120 nm thick was first sputter deposited onto a substrate (*e.g.*, silicon wafer or glass slide) using an $Ag_{82.5}Au_{17.5}$ (atomic percentage) alloy target. A monolayer of 460–1100 nm size polystyrene beads (PS) was then formed on top of the alloy film. In our experience, over 90% of the alloy surface covered with close-packed PS beads can be achieved reproducibly (Scheme 1a). Next, a timed oxygen plasma treatment was employed to shrink the PS beads, thus separating them from neighboring beads. The sample was then sputter-etched in argon plasma to transfer the bead pattern into the alloy film (Scheme 1b). Once the pattern transfer was completed, the PS beads were removed (Scheme 1c). The alloy disks were dealloyed in concentrated nitric acid, followed by rinsing in deionized (DI) water (Scheme 1d) to produce the *array* format NPG disks. There was substantial size shrinkage during the PS bead etching step as well as the dealloying process. Scanning electron microscopy (SEM) images (Scheme 1e–h) show the corresponding nanostructures through the fabrication steps. To produce suspended colloidal NPG disks, high-density NPG disk arrays on a 3 inch Si wafer were further sonicated in DI water.

Fig. 1 shows SEM images of monolayer samples of NPG disks on Si substrates. The mean size and the standard deviation of different NPG disks are determined by measuring ~100 disks using SEM images for each set of samples. The NPG disks obtained by using PS beads with original sizes of 460 ± 9600 ± 12 800 ± 9 and 1100 ± 14 nm were 300 ± 7400 ± 10 500 ± 6 and 700 ± 13 nm in diameter, respectively. The small size dispersion confirms the high fidelity of our pattern-transfer process. Compared to the original sizes of the PS beads, there is an approximately 33–37% decrease in the NPG disk diameter, of which ~5% occurs during the oxygen plasma treatment and up to 32% occurs during the dealloying process. The thickness also shrank from 120 to 75 nm. These values are consistent with ~30% volume reduction by electrochemical dealloying of Au–Ag alloys because of plastic deformation.[22] Simulations of geometric relaxation in bicontinuous nanoporous metals revealed that surface relaxation played a significant role in the dramatic shrinkage during selective dissolution.[23] Recently, a similar size shrinkage of ~29% was reported by Dong and coworkers after dealloying of the Au–Ag alloy ($Ag_{77}Au_{23}$, at%) in nitric acid.[24]

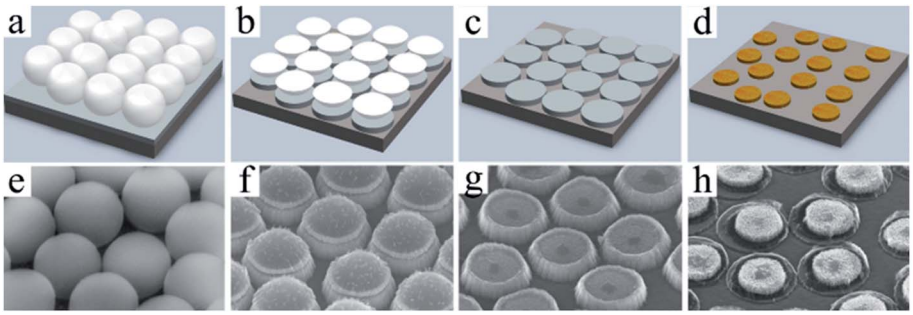

Scheme 1 (a–d) Illustration of the fabrication process used to prepare NPG disks on a silicon (or glass) substrate: (a) formation of a monolayer of polystyrene (PS) beads on an alloy-coated silicon (or glass) substrate; (b) O_2 plasma shrinkage of the PS beads and Ar sputter etching to form isolated alloy disks; (c) selective dissolution of PS beads by chloroform; (d) formation of NPG disks by dealloying. Figures (e to h) are SEM images taken at each step of the process with a 45° viewing angle.

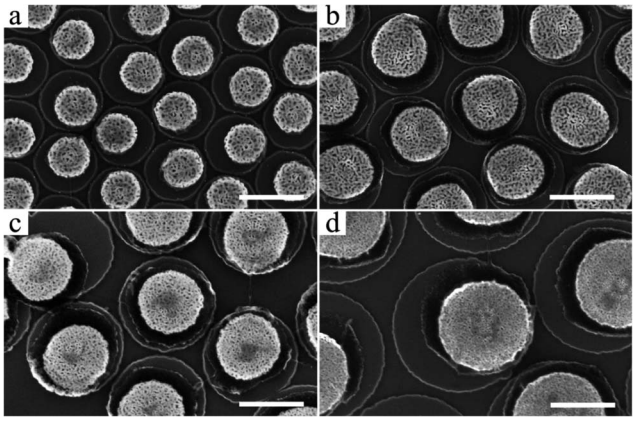

Fig. 1 SEM images of NPG disks made using 460 ± 9600 ± 12 800 ± 9 and 1100 ± 14 nm PS beads on Si substrates. The corresponding diameters are (a) 300 ± 7, (b) 400 ± 10, (c) 500 ± 6 and (d) 700 ± 13 nm, respectively. The scale bar is 500 nm.

NPG disks can move off-site during dealloying, as indicated by the presence of off-centered NPG disks with respect to the silicon etch marks during the Ar sputter-etching step. We note that the adhesion between Si and the sputtered Au–Ag alloy was weakened due to the oxidation of silicon to SiO_2 by concentrated nitric acid.[25] Therefore, the strong stress generated by volume shrinkage plausibly led to movement of the NPG disks.[26] NPG disks were easily released from the Si substrate by sonication due to the weak adhesion, which was nevertheless sufficiently strong to hold the disks in place while rinsing with water. Furthermore, the "unconstrained" shrinkage led to crack-free NPG, in contrast to NPG disks that were strongly immobilized on Au substrates in our previous study.[20] Crack-free NPG disks are essential for preserving the monolithic structural integrity during and after the release process, as well as the uniformity of the nanoporous network. The corresponding pore sizes for the 300–700 nm diameter NPG disks were 13.8 ± 2.2, 13.7 ± 2.9, 12.5 ± 2.0 and 12.8 ± 2.4 nm, respectively (Table 1). The total surface area was about seven-fold the projected geometrical area with a pore size of ~13 nm by SEM image analysis based on ImageJ (see Table 1).[20,27]

Non-aggregating NPG disks

Fig. 2 displays three different views of NPG disks to further show the capability of preparing both the arrayed and colloidal NPG disks. Fig. 2a and b show high-density NPG disk arrays on a 3 inch Si wafer and the SEM image of a single NPG disk, respectively. With the aid of sonication, NPG disks were released from the substrates into DI water to form colloidal NPG disk suspensions (Fig. 2c). The inset shows colloidal NPG disks dried on a Si wafer. To our surprise, *surfactant-free* NPG disks were easily transferred into DI water without aggregation. Therefore, by flowing individual colloidal NPG disks in microfluidic channels, the single disk (400 nm diameter) buoyant mass was determined to be $6.04 \times 10^{-14} \pm 7.6 \times 10^{-15}$ g as shown in Fig. 2d. For comparison, we also fabricated 400 nm diameter Au disks without porous structures through nearly identical procedures. These Au disks immediately formed aggregates in the millimeter size range in an aqueous solution upon release from the substrates. To understand the unique colloidal stability of the NPG disks, we measured their zeta potentials to elucidate their surface charge state (see Table 1).[28,29] In general, when the absolute value of the zeta potential is larger than 25 mV, a nanoparticle suspension has a high degree of stability due to strong electrostatic repulsion between particles.[28] The zeta potentials of the 300 and 400 nm NPG disks were −28.5 ± 2.1 and −26.4 ± 3.2 mV, respectively, suggesting that both sizes of colloidal NPG disks had negatively charged surfaces and were quite stable in solution, which was consistent with our observations. Although the 500 and 700 nm diameter NPG disks possess negative surface charges but with slightly smaller zeta potentials, these larger NPG disks also exhibit practically useful long-term stability (*i.e.*, no/minimal aggregation when stored in DI water at 4 °C for 4 months).

The observed negative surface charge could be explained by the presence of deprotonated hydroxyl groups at the surface of NPG disks in aqueous solutions, which would plausibly form during the dealloying process in nitric acid. Hydroxyl groups formed on metal or metal oxide surfaces exhibit a stretching band at 3710 cm^{-1} in infrared (IR) spectroscopic analysis.[30] As shown in Fig. S1,† the observed OH stretching band of dried 400 nm NPG disks at 3710 cm^{-1} was consistent with the presence of hydroxyl groups on the surface of NPG disks.

Table 1 The average diameter, pore size, roughness factor, and zeta potentials (ζ) of the as-prepared NPG disks. The thickness of the NPG disks was 75 ± 1 nm

NPG disk samples[a]	Average diameter (nm)	Average pore size (nm)	Roughness factor[b]	ζ (mV)[c]	FWHM of the in-plane peak[d] (nm)
1	300 ± 7	13.8 ± 2.2	6.56 ± 0.38	−28.5 ± 2.1	421.9
2	400 ± 10	13.7 ± 2.9	7.38 ± 0.41	−26.4 ± 3.2	460.9
3	500 ± 6	12.5 ± 2.0	7.71 ± 0.11	−19.0 ± 1.3	717.6
4	700 ± 13	12.8 ± 2.4	7.65 ± 0.27	−22.7 ± 1.2	1329.8

[a] NPG disks were made by using 460, 600, 800 and 1100 nm PS beads as masks and identical alloy thickness. [b] The roughness factor was obtained by using the expression $3h\beta/r$, where h, β, and r are the NPG disk thickness, 2-dimensional porosity, and mean pore radius, respectively. The analysis was based on ImageJ (http://rsbweb.nih.gov/ij/). [c] Zeta potentials were measured in DI water. [d] The full width at half maximum (FWHM) of the in-plane peaks of NPG disks obtained in air ($n = 1$) was measured by GRAMS/AI.

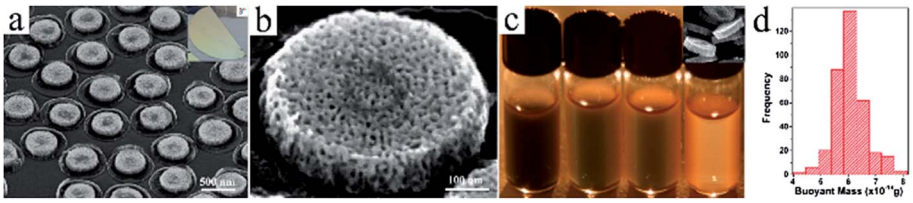

Fig. 2 SEM images of NPG disks taken at a 45° viewing angle, stored in DI water, and single disk buoyant mass measurements: (a) high-density NPG disk arrays on Si wafer before release. The inset is a 3″ silicon wafer covered by a high-density monolayer of PS beads. (b) A single NPG disk with a diameter of 500 nm. (c) NPG disks having different sizes 300 ± 7, 400 ± 10, 500 ± 6, and 700 ± 13 nm (from left to right) after being released from the substrates by sonication in DI water to form colloidal NPG disk suspensions. The inset is the SEM image of NPG disks released from the substrate by sonication, dropped and dried on a Si wafer. (d) Histogram of 400 nm NPG disk buoyant mass distribution measured by flowing colloidal NPG disks in the microfluidic channel, with an average of $6.04 \times 10^{-14} \pm 7.6 \times 10^{-15}$ g.

Inter-particle van der Waals forces are known to be affected by surface roughness and geometric factors, where the surface roughness minimizes van der Waals interaction by limiting the contacts between the particles.[31] In the case of NPG disks, where the surfaces are unquestionably rough, the aggregation could also be suppressed by reduced van der Waals forces. Therefore, NPG disks exhibit much greater stability than Au disks because of their negative surface charge and their unique nanoporous structures. Their superior stability and potential for facile surface modification/functionalization would offer a wide range of applications in a variety of fields ranging from biosensing and drug delivery to catalysis and plasmonics.

NPG disks' composition

In the past few years, various NPG material parameters have been extensively studied, including grain size and boundaries by X-ray diffraction,[32] crystal-facet orientations by high-resolution TEM (HRTEM),[12] and atomic composition by X-ray photoelectron spectroscopy (XPS).[33,34] NPG materials are known to contain residual silver content and other process-associated or environmental substances, and can be characterized by XPS, which is sensitive to the top ~10 nm of non-porous substrates.[35] Fig. S2† shows the XPS spectrum from 0 to 1200 eV of NPG disks drop-coated on a Si wafer, where the major peaks originated from Au and Ag and other elements such as Si, O, N and C also appear. The Si wafer as well as the surface layer of SiO_2 on the wafer mainly contributed to Si and O. Trace amounts of nitrogen are observed, and the peak of N 1s at 400.2 eV can be assigned to N^- in metal–N species formed during the sputter etching.[36] The XPS spectrum indicates that the porous structures of NPG disks generated by concentrated nitric acid had a clean surface except for minor surface contamination by carbon, which could plausibly come from the environment.

The chemical states of the NPG disks can also be identified by XPS. The Ag 3d peaks of NPG disks are shown in Fig. S3a.† The binding energy of $3d_{5/2}$ was 367.9 eV, slightly lower than that of metallic Ag (368.3 eV). The shift to lower binding energy is typical for the oxidized Ag species.[33,37] The oxidation of Ag likely occurred during the dealloying process. In addition, rehybridization effects in the Au–Ag alloy that reduce the electron density of silver could also lead to lower Ag binding energies.[33] For Au, both the peak shapes and the Au 4f binding energies ($4f_{5/2}$ 83.9 and $4f_{7/2}$ 87.6 eV) were consistent with a metallic state. XPS surface compositional analysis revealed that ~24% residual Ag remains on the surface of the NPG disks. Segregation of Ag from the bulk to the surface region is known to occur in metal alloys.[38] Consequently, NPG disks exhibit a clean surface with little contamination and negligible interference from residual silver, which can be important for sensing, SERS and catalysis applications.

NPG disk plasmonics

The plasmonic properties of NPG disks can be first understood by comparing with semi-infinite NPG thin films. As shown in the extinction spectra in Fig. 3a, three peaks have been assigned to NPG LSPR ("▲"), out-of-plane resonance ("■"), and in-plane resonance ("●"). The NPG LSPR mode originated from the nanoporous structures, whereas the in-plane and out-of-plane modes were associated with the external disk shape. Size-dependent plasmonic shifts in these peaks have been observed when the disk diameter was increased from 300 to 700 nm. Among these peaks, the in-plane resonance clearly dominates and *only* exists in NPG disks but *not* in semi-infinite NPG thin films, which will be further discussed later. According to Chen and coworkers, NPG thin films exhibited two plasmonic resonance peaks near 490 and 515 nm in air. While the 490 nm peak assigned to out-of-plane resonance ("■") was nearly fixed, the peak at 515 nm assigned to NPG LSPR ("▲") exhibited limited tunability with respect to pore size and ambient refractive index.[16] A red shift of this peak to 540 nm in air was observed when the pore size was varied from 10 to 30 nm.[16] In contrast, NPG disks have highly tunable plasmonic properties for all peaks as shown in Fig. 3a, due to plasmonic coupling between the nanoporous structures and the patterned disk shape. Also according to Chen's work,[16] unpatterned NPG thin films with a pore size of ~13 nm should exhibit an NPG LSPR peak ("▲") between 510 and 530 nm in air. However, with 13 nm pore size, this peak shifted to ~600 nm and nearly 800 nm for NPG disks with a diameter of 300 and 500 nm, respectively (Fig. 3b). In addition, the out-of-plane resonance mode ("■"), though fixed in NPG thin films, became mobile and shifted from 552 nm to 706 nm as the diameter increased from 400 to 700 nm. The peak positions *versus* NPG disk diameters in air are summarized in Fig. 3b.

The plasmonic properties of NPG disks can be further understood by comparing with those of Au disks having the

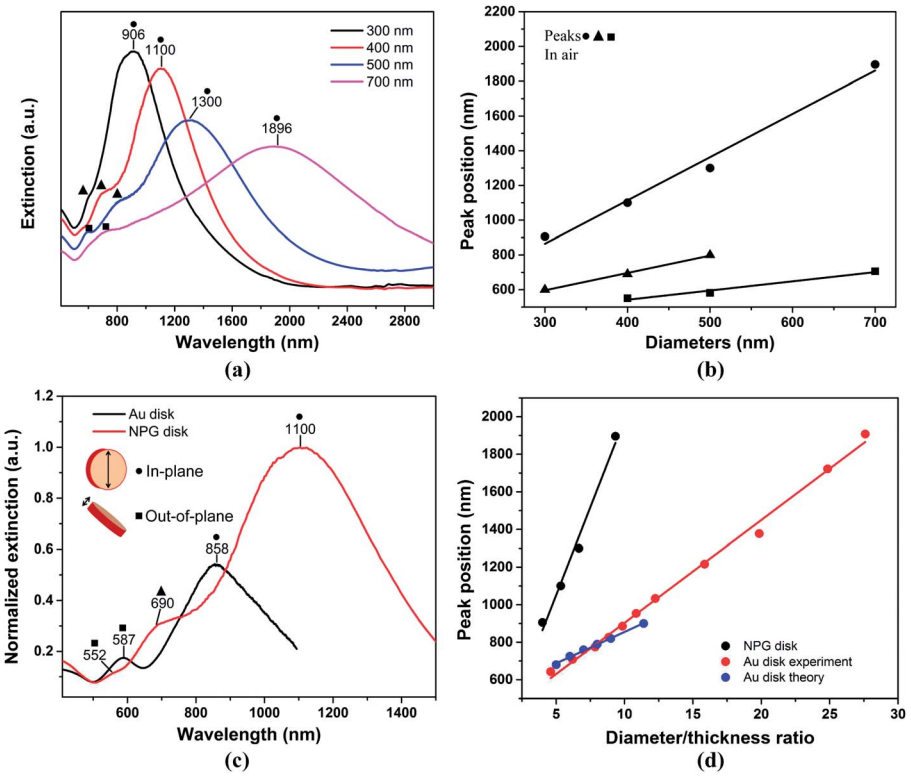

Fig. 3 Size-dependent plasmonic properties of NPG disk and comparison with Au disk: (a) extinction spectra of NPG disks with different diameters: 300, 400, 500, and 700 nm. The samples consisted of high-density NPG disk monolayers on glass substrates in air ($n = 1$). (b) Plasmonic resonance peak positions *versus* NPG disk diameters in air. (c) Extinction spectra of 400 nm diameter and 75 nm thickness Au disks and NPG disks on glass substrates measured in air. Both spectra were normalized to buoyant mass. The inset shows the in-plane and out-of-plane resonance modes. (d) The in-plane dipole resonance peak positions are plotted as a function of the diameter/thickness ratio. The black circle represents NPG disks. The red and blue circles correspond to experimental results[39] and theoretical calculations,[40] respectively. All extinction spectra were collected at 0° normal incidence.

same diameter and thickness on glass substrates (Fig. 3c). The two Au disk absorption peaks at 858 and 587 nm are assigned to the in-plane ("●") and out-of-plane ("■") resonance modes, respectively.[41] At normal incidence, it is noted that the out-of-plane resonance mode begins to appear when the Au disk diameter size is larger than 250 nm (thickness ~20 nm).[39] With the large diameter, the Au disk and NPG disk exhibit the out-of-plane resonance mode around 500–600 nm that agrees with the previous report. For NPG disks, as mentioned previously, there are three peaks at 1100, 690 and 552 nm. The peaks at 1100 and 552 nm correspond to the in-plane ("●") and out-of-plane ("■") resonance modes due to the disk shape, respectively, while the additional peak at 690 nm originates from the NPG LSPR ("▲") generated by the nanopores and nanoscale Au ligaments.[16] Compared to Au disks, the plasmonic bands of NPG disks exhibit a remarkable red shift (*i.e.*, the in-plane resonance) from 858 to 1100 nm. It could be interpreted by plasmonic coupling (or plasmon hybridization) that has been well studied.[42–44] As for simple metal nanoparticles, plasmonic coupling gives rise to a red shift in the plasmon as the distance between two nanoparticles decreases.[42–44] However, in the case of NPG disks, the distances between disks on the substrates are random in the region from 0.1 to 1 μm, and thus the coupling effect caused by the inter-disk distances is greatly reduced. The red shift must have been caused by coupling between the 3-dimensional bicontinuous porous nanostructures and the outer geometrical size and shape. Such coupling is observed as spectral overlap between the in-plane resonance and the NPG LSPR. By normalizing the extinction spectra to their respective buoyant mass measured on a single-particle basis (Fig. 2d), we found that the peak height of the in-plane mode of NPG disks is about twice that of Au disks of the same external geometry. The NPG disk also shows a much broader in-plane peak compared to the Au disk; 460.9 *versus* 284.0 nm for the full width at half maximum (FWHM). Overall, the total extinction per buoyant mass for NPG disks is 3.3 times that of Au disks. The peak broadening can be attributed to random nanoporous structures and nanoscale Au ligaments.

Since it is known that Au disks exhibit a size-dependent shift in one or more of the plasmonic resonance peaks due to the changes in electromagnetic retardation,[39] we expect to see similar behavior in NPG disks. As shown in Fig. 3b, the UV-vis-NIR extinction spectra of NPG disks of different sizes indicate that the in-plane dipole resonance mode ("●") red shifted from 906 to 1896 nm when the disk diameter was increased from 300 to 700 nm. For Au disks, previous results revealed that the red shift of the in-plane resonance mode peak was around 40 nm per diameter-to-thickness ratio (DTR) ($d\lambda/dDTR$).[39,40] In

contrast, NPG disks exhibit a 4.5 times larger dλ/dDTR of 187 nm than that of Au disks, suggesting larger tunability by geometrical modifications. Peak positions *vs.* DTR for NPG disks and Au disks are shown in Fig. 3d. As alluded previously, another feature of NPG disks is the peak broadening compared to Au disks as the diameter increases from 300 to 700 nm (Table 1). Besides the in-plane resonance peak ("●"), the out-of-plane ("■") and NPG LSPR ("▲") peaks have qualitatively similar red shifts as the diameter increases. This has never been observed in NPG-related materials discussed previously.

Next, we discuss the variability of NPG disk plasmon resonance due to refractive index changes in the ambient environment. It is well known that the plasmon resonance is sensitive to the surrounding medium and exhibits peak shifts, which can be quantified by a sensitivity factor dλ/dn with the units of nm per refractive index unit (nm per RIU). We examined the plasmonic properties of NPG disks and Au disks in water ($n = 1.33$). The extinction spectra shown in Fig. 4a suggest that the sensitivity factor dλ/dn for the NPG LSPR peak ("▲") of 400 nm NPG disks was ~456 nm, much larger than those observed for NPG thin films. Indeed, the unique nanoporous structure makes NPG disks more sensitive to the surrounding medium than either Au disks or unpatterned NPG thin films. To observe the NPG LSPR and the out-of-plane peaks more clearly, the 410–980 nm regions of Fig. 3a and 4a are reproduced in Fig. S4a and S4b,† respectively. As shown in Fig. 4b, the peaks of the in-plane resonance modes exhibited a dλ/dn of 190 and 518 nm per RIU for Au disks and NPG disks by changing the ambient environment from air to water, respectively. The out-of-plane dipole resonance mode of Au disks at 587 nm did not shift, while that of the NPG disks still red shifted, with a dλ/dn of ~152 nm per RIU.

NPG disks can be used as plasmonic sensors due to the excellent sensitivity factor. To further extend the range of index sensing into those for common solvents, we investigated the peak shifts of 400 nm NPG disks over the index range of 1.36 to 1.495 using pure ethanol, ethanol–toluene mixtures and pure toluene. Fig. 5a illustrates the extinction spectra of the 400 nm NPG disks in these various solvents. As quantified in Fig. 5b, the peaks "●" and "■" red shifted with sensitivity factors of 869.5 and 235.4 nm per RIU, respectively. The peak shift in the NPG LSPR peak was unclear due to the overlap with the broad peak "●". Overall, the sensitivity of the NPG disk in-plane peak

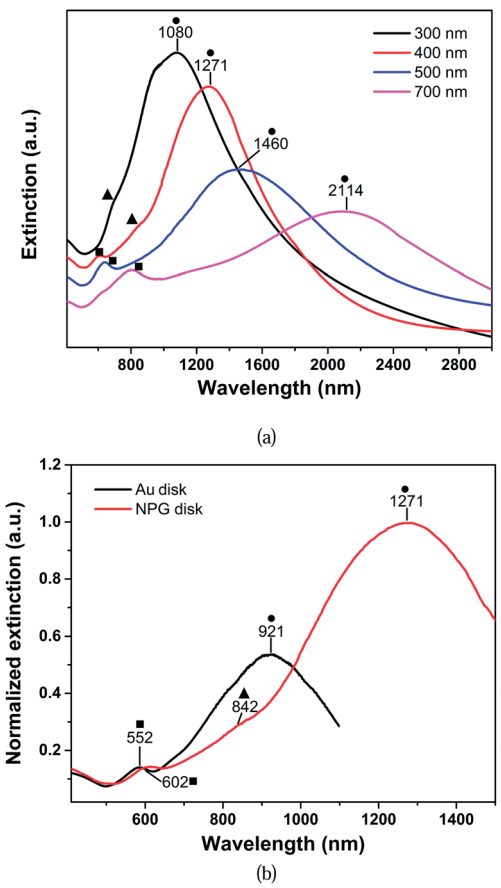

Fig. 4 (a) Extinction spectra of NPG disks with different diameters: 300, 400, 500, and 700 nm in water ($n = 1.33$). (b) Extinction spectra normalized to the buoyant mass of 400 nm diameter and 75 nm thickness Au disks and NPG disks on glass substrates measured in water.

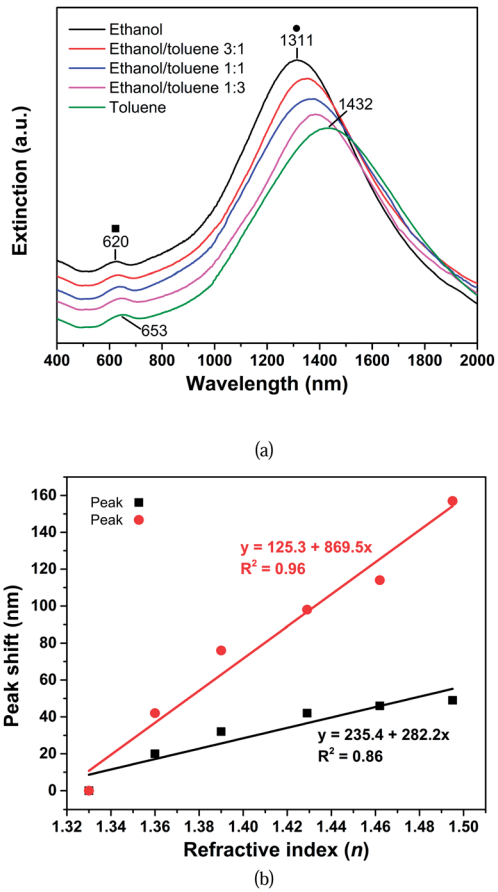

Fig. 5 (a) Extinction spectra of 400 nm NPG disks in various solvent mixtures with known refractive indices (n) varying from 1.36 to 1.495: ethanol ($n = 1.36$), 3 : 1 ethanol–toluene ($n = 1.39$), 1 : 1 ethanol–toluene ($n = 1.429$), 1 : 3 ethanol–toluene ($n = 1.462$), and toluene ($n = 1.495$).[16] (b) The peak shifts of peaks marked with symbols ● and ■ are plotted *versus* n.

("●") is larger than those of spherical Au nanoparticles, Ag@Au nanoshells, SiO_2@Au nanoshells, Au disks, Au nanorods, nanocages and silver nanoprisms,[16,45–48] and comparable to nanorices and nanorings which range up to 800 nm per RIU.[49,50]

To further elucidate the observed extraordinary size and environment-dependent plasmonic behavior of NPG disks, we performed finite difference time domain (FDTD) simulations and compared with Au disks having identical external shape parameters: 500 nm in diameter and 75 nm in thicknesses. The NPG disk model shown in Fig. 6a was constructed directly from the SEM image shown previously. Fig. 6c displays the calculated electric-field (E-field) distribution for the 1300 nm incident wavelength, matching the in-plane resonance previously discussed. "Hot-spots" in the pores around the edges are observed with a maximum E-field enhancement factor of ~100. In contrast, the Au disk in Fig. 6b produced a maximum E-field enhancement of ~15, confined to either side of the disk (Fig. 6d). Next, we examined the E-field distribution of NPG disk for the 785 nm incident wavelength, matching the NPG LSPR peak previously discussed. As shown in Fig. 6e, uniformly distributed hot-spots within the entire disk are observed with a maximum E-field enhancement factor of about 32. In contrast, the E-field distribution of Au disk as shown in Fig. 6f appears similar to that in Fig. 6d with a maximum enhancement factor of about 6. Thus, the NPG disk maintains a ~6-fold higher E-field enhancement compared to the Au disk.

The different patterns of hot-spot distribution in the NPG disk for 1300 and 785 nm incident wavelengths are most intriguing (Fig. 6c and e). At 1300 nm, the hot-spot distribution appears to be concentrated near the pores around edges, supporting our previous interpretation of coupling between the in-plane resonance and the pores around edges. In contrast, the uniform hot-spot distribution for 785 nm supports the interpretation that it is NPG LSPR. Of course, coupling was still

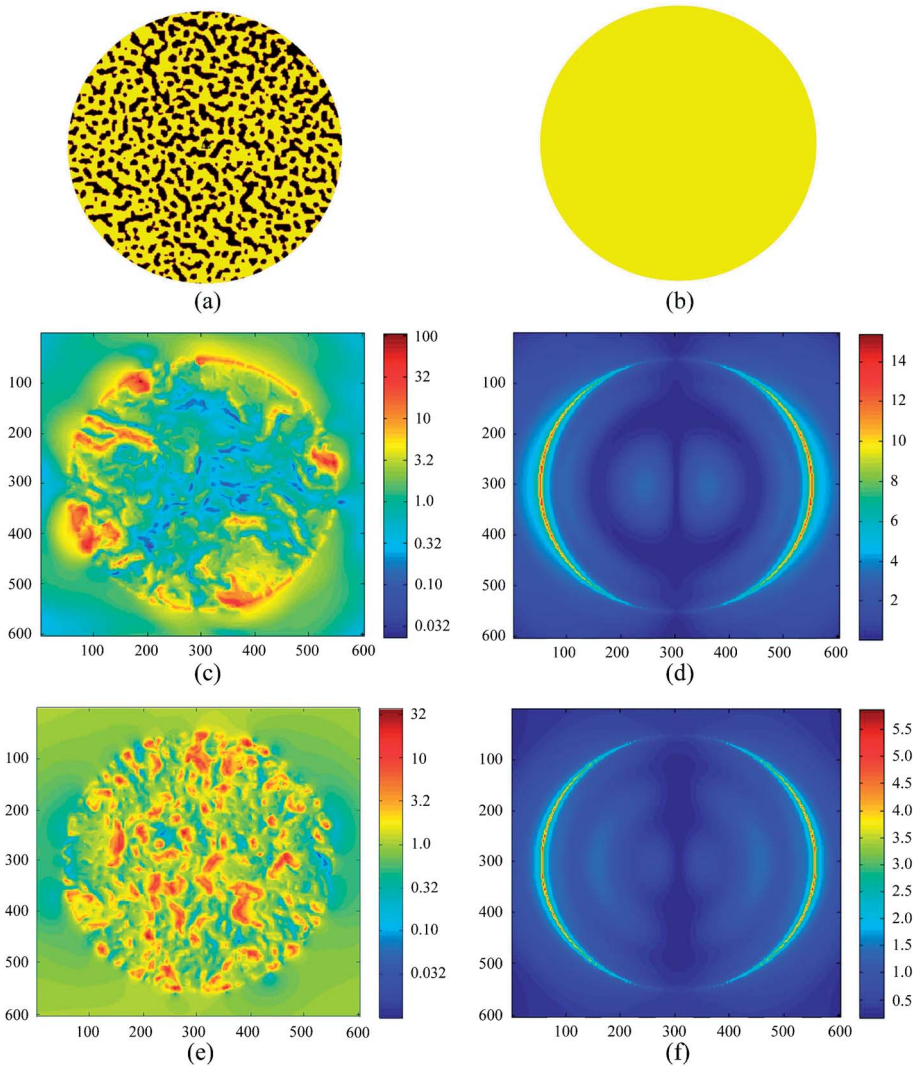

Fig. 6 E-field distribution of the NPG disk and Au disk with 500 nm diameter and 75 nm thickness: (a) and (b) are simulated models for NPG disk and Au disk, respectively. The E-field distribution was simulated using FDTD with plane wave incidence perpendicular to the disks, horizontally polarized. (c and d) E-field distribution of the NPG disk and Au disk for the 1300 nm incidence wavelength, respectively. (e and f) E-field distribution of the NPG disk and Au disk for the 785 nm incidence wavelength, respectively.

present since the NPG LSPR sits on the tail of the in-plane resonance mode (see Fig. 3a). The 785 nm results also shed new light on our previous observation of excellent SERS with an enhanced factor exceeding 10^8 by 785 nm excitation.[20] Overall, the FDTD results provide further support that the plasmonic coupling originating from the random nanoporous structure and the disk shape plays a key role in the unique plasmonic properties of NPG disks.

Conclusions

In summary, we have demonstrated shape and size-controlled monolithic NPG disks as a new type of plasmonic nanoparticle in both substrate-bound and non-aggregating colloidal formats. NPG disks feature a large specific surface area due to their internal nanoporous network. NPG disks also contain numerous plasmonic hot-spots throughout the internal volume, which has enabled the demonstration of the high LSPR sensitivity to ambient index changes. Putting NPG disks into the context of the existing repertoire of gold nanoparticles, which permits tunability by varying parameters in design dimensions such as material composition, particle size, shape (*e.g.*, sphere, rod, cube, triangle, and cage) and configuration (core–shell), our work strongly advocates porosity as yet another potential design dimension for plasmonic engineering. In addition to its excellent plasmonic properties, the gold material permits facile binding of a wide range of thiolated molecular and biomolecular species through the Au–S bond. The synergy of large specific surface area, high-density hot spots, and tunable plasmonics would profoundly impact applications where plasmonic nanoparticles and non-plasmonic mesoporous nanoparticles are currently employed, *e.g.*, in *in vitro* and *in vivo* biosensing, molecular imaging, photothermal contrast agents, and molecular cargos.

Experimental

Preparation of the polystyrene bead (PS bead) monolayer

The assembled monolayer of PS beads on a large scale area was prepared using a modification of a previously reported procedure.[51,52] Briefly, the purchased PS beads were further purified by centrifugation with a mixture of ethanol and DI water (1 : 1, volume ratio), and then dried in an oven at 50 °C for 24 h. A 1% PS beads solution (weight ratio) was then prepared by redispersing the dried PS beads in the water–ethanol solution (1 : 1 volume ratio). The 120 nm thick Au–Ag alloy film was deposited on substrates such as 3″ silicon wafers and the micro-coverglass using an $Ag_{82.5}Au_{17.5}$ alloy target, and then the substrate was first placed in a Petri dish (3.5″ in diameter) containing DI water. The as-prepared PS bead solution was slowly injected at the air–water interface with a syringe pump at a rate of 50 μL min^{-1}. The monolayer of PS beads spontaneously formed at the air–water interface. Formation of the highly patterned monolayer was further driven by the addition of 5 mM sodium dodecyl sulfate aqueous solution on the water surface. Finally, the assembled monolayer was transferred onto a substrate with the alloy film by carefully lifting it out from the air–water interface and then dried at room temperature.

Fabrication of NPG disks

The Au–Ag alloy film covered with the PS bead monolayer was first etched in oxygen plasma between 2 and 5 min to shrink the PS beads (2 min for 460 nm PS beads, 3 min for 600 and 800 nm PS beads, and 5 min for 1100 nm PS beads). The pressure and power were 30 mTorr and 100 W, respectively. After treatment with oxygen plasma, the sample was further etched in a 2 mTorr per 100 W argon plasma for 12 min to obtain Au–Ag alloy disks. The remaining polystyrene was removed by sonication in chloroform for 1 min. Finally, the NPG disks were formed by dealloying Ag in 70% nitric acid for 1 min. The sample was washed in DI water to remove the dealloying reaction products and excess nitric acid.

Author contributions

F.S.Z. and J.B.Z. developed part of the fabrication process, performed fabrication, designed and performed experiments, analyzed data and equally contributed to the work. J.B.Z. wrote part of the paper. M.M.P.A., P.S., and J.Q. performed FDTD calculations and 2-dimensional porosity analysis. P.M., M.G., J.C.W., and W.C.S. designed and developed part of the fabrication process. C.H.L. performed XPS. C.H.L. and T.R.L. interpreted the XPS data. A.P., U.S. and B.R. performed zeta potential and buoyant mass measurements. T.R.L., R.C.W., and J.C.W. provided domain-specific knowledge and edited the paper. W.C.S. conceived the idea, designed the fabrication process, envisioned the experiments and characterization methods, provided guidance in data analysis, wrote the paper, and directed the research.

Conflict of interest

The authors declare no competing financial interest.

Acknowledgements

F.S.Z. thanks Dr Bradley and Dr Chang from the Nanofabrication Facility at the University of Houston for training and trouble-shooting. F.S.Z., J.B.Z. and W.C.S. thank Dr Cynthia Shen at Halliburton for assistance in measuring extinction spectra. T.R.L. thanks the Robert A. Welch Foundation (Grant no. E-1320), the AOARD (no. 134032), and the Texas Center for Superconductivity for generous support. R.C.W. and U.S. thank the Welch Foundation (Grant no. E-1264). J.C.W. acknowledges the generous support of The Cullen Foundation through a Hugh Roy and Lillie Cranz Cullen Distinguished University Professorship and the Texas Center for Superconductivity at the University of Houston (TCSUH). W.C.S. acknowledges the National Science Foundation (NSF) CAREER Award (CBET-1151154), National Aeronautics and Space Administration (NASA) Early Career Faculty Grant (NNX12AQ44G) and a grant from the Gulf of Mexico Research Initiative (GoMRI-030).

References

1 W. L. Barnes, A. Dereux and T. W. Ebbesen, *Nature*, 2003, **424**, 824–830.
2 J. N. Anker, W. P. Hall, O. Lyandres, N. C. Shah, J. Zhao and R. P. Van Duyne, *Nat. Mater.*, 2008, **7**, 442–453.
3 H. A. Atwater and A. Polman, *Nat. Mater.*, 2010, **9**, 205–213.
4 J. R. Krenn, *Nat. Mater.*, 2003, **2**, 210–211.
5 E. Ringe, B. Sharma, A.-I. Henry, L. D. Marks and R. P. Van Duyne, *Phys. Chem. Chem. Phys.*, 2013, **15**, 4110–4129.
6 J. F. Li, Y. F. Huang, Y. Ding, Z. L. Yang, S. B. Li, X. S. Zhou, F. R. Fan, W. Zhang, Z. Y. Zhou, Y. WuDe, B. Ren, Z. L. Wang and Z. Q. Tian, *Nature*, 2010, **464**, 392–395.
7 G. A. Sotiriou, *Wiley Interdiscip. Rev.: Nanomed. Nanobiotechnol.*, 2013, **5**, 19–30.
8 Y. B. Zheng, B. Kiraly, P. Weiss and T. Huang, *Nanomedicine*, 2012, **7**, 751–770.
9 K. L. Kelly, E. Coronado, L. L. Zhao and G. C. Schatz, *J. Phys. Chem. B*, 2002, **107**, 668–677.
10 A. Wittstock, J. Biener, J. Erlebacher and M. Bäumer, *Nanoporous Gold: From an Ancient Technology to a High-Tech Material*, Royal Society of Chemistry; 2012.
11 A. Wittstock, V. Zielasek, J. Biener, C. M. Friend and M. Bäumer, *Science*, 2010, **327**, 319–322.
12 T. Fujita, P. Guan, K. McKenna, X. Lang, A. Hirata, L. Zhang, T. Tokunaga, S. Arai, Y. Yamamoto and N. Tanaka, *Nat. Mater.*, 2012, **11**, 775–780.
13 Y. Ding and M. Chen, *MRS Bull.*, 2009, **34**, 569–576.
14 F. Yu, S. Ahl, A.-M. Caminade, J.-P. Majoral, W. Knoll and J. Erlebacher, *Anal. Chem.*, 2006, **78**, 7346–7350.
15 J. Biener, G. W. Nyce, A. M. Hodge, M. M. Biener, A. V. Hamza and S. A. Maier, *Adv. Mater.*, 2008, **20**, 1211–1217.
16 X. Lang, L. Qian, P. Guan, J. Zi and M. Chen, *Appl. Phys. Lett.*, 2011, **98**, 093701–093703.
17 J. D. Ryckman, Y. Jiao and S. M. Weiss, *Sci. Rep.*, 2013, 3.
18 H. Liu, L. Zhang, X. Lang, Y. Yamaguchi, H. Iwasaki, Y. Inouye, Q. Xue and M. Chen, *Sci. Rep.*, 2011, 1.
19 J.-S. Wi, S. Tominaka, K. Uosaki and T. Nagao, *Phys. Chem. Chem. Phys.*, 2012, **14**, 9131–9136.
20 J. Qi, P. Motwani, M. Gheewala, C. Brennan, J. C. Wolfe and W.-C. Shih, *Nanoscale*, 2013, **5**, 4105–4109.
21 X. Lang and M. Chen, in *Nanoporous Gold: From an Ancient Technology to a High-Tech Material*, ed. Arne Wittstock, *et al.*, Royal Society of Chemistry, 2012, ch. 6.
22 S. Parida, D. Kramer, C. Volkert, H. Rösner, J. Erlebacher and J. Weissmüller, *Phys. Rev. Lett.*, 2006, **97**, 035504.
23 D. A. Crowson, D. Farkas and S. G. Corcoran, *Scr. Mater.*, 2007, **56**, 919–922.
24 D. Wang and P. Schaaf, *J. Mater. Chem.*, 2012, **22**, 5344–5348.
25 M. Steinert, J. Acker, S. Oswald and K. Wetzig, *J. Phys. Chem. C*, 2007, **111**, 2133–2140.
26 Y. Sun and T. J. Balk, *Metall. Mater. Trans. A*, 2008, **39**, 2656–2665.
27 S. Erkin, B. Yevgeny, R. B. Matthew, L. R. Michael, J. S. Kevin and L. Y. Martin, *Nanotechnology*, 2010, **21**, 125504.
28 J. S. Reed, *Introduction to the Principles of Ceramic Processing*, John Wiley & Sons, New York, 2nd edn, 1995.
29 R. Xu, *Particuology*, 2008, **6**, 112–115.
30 S. Haukka, E.-L. Lakomaa and T. Suntola, *Stud. Surf. Sci. Catal.*, 1999, **120**, 715–750.
31 J. Visser, *Powder Technol.*, 1989, **58**, 1–10.
32 S. V. Petegem, S. Brandstetter, R. Maass, A. M. Hodge, B. S. El-Dasher, J. r. Biener, B. Schmitt, C. Borca and H. V. Swygenhoven, *Nano Lett.*, 2009, **9**, 1158–1163.
33 A. Wittstock, B. r. Neumann, A. Schaefer, K. Dumbuya, C. Kübel, M. M. Biener, V. Zielasek, H.-P. Steinrück, J. M. Gottfried, J. r. Biener, A. Hamza and M. Bäumer, *J. Phys. Chem. C*, 2009, **113**, 5593–5600.
34 L. Zhang, L. Chen, H. Liu, Y. Hou, A. Hirata, T. Fujita and M. Chen, *J. Phys. Chem. C*, 2011, **115**, 19583–19587.
35 B. D. Ratner and D. G. Castner, *Surface Analysis-The Principal Techniques*, 2009, 2nd edn., pp. 47–112.
36 J. Baltrusaitis, P. M. Jayaweera and V. H. Grassian, *Phys. Chem. Chem. Phys.*, 2009, **11**, 8295–8305.
37 G. B. Hoflund, Z. F. Hazos and G. N. Salaita, *Phys. Rev. B: Condens. Matter Mater. Phys.*, 2000, **62**, 11126–11133.
38 V. Zielasek, B. Jürgens, C. Schulz, J. Biener, M. M. Biener, A. V. Hamza and M. Bäumer, *Angew. Chem., Int. Ed.*, 2006, **45**, 8241–8244.
39 I. Zorić, M. Zäch, B. Kasemo and C. Langhammer, *ACS Nano*, 2011, **5**, 2535–2546.
40 Y.-C. Chang, H.-C. Chung, S.-C. Lu and T.-F. Guo, *Nanotechnology*, 2013, **24**, 095302.
41 Y. B. Zheng, B. Kiraly, S. Cheunkar, T. J. Huang and P. S. Weiss, *Nano Lett.*, 2011, **11**, 2061–2065.
42 W. Rechberger, A. Hohenau, A. Leitner, J. Krenn, B. Lamprecht and F. Aussenegg, *Opt. Commun.*, 2003, **220**, 137–141.
43 N. J. Halas, S. Lal, S. Link, W.-S. Chang, D. Natelson, J. H. Hafner and P. Nordlander, *Adv. Mater.*, 2012, **24**, 4842–4877.
44 B. K. Juluri, N. Chaturvedi, Q. Z. Hao, M. Q. Lu, D. Velegol, L. Jensen and T. J. Huang, *ACS Nano*, 2011, **5**, 5838–5847.
45 Y. Sun and Y. Xia, *Anal. Chem.*, 2002, **74**, 5297–5305.
46 P. Hanarp, M. Käll and D. S. Sutherland, *J. Phys. Chem. B*, 2003, **107**, 5768–5772.
47 M. Hu, J. Chen, M. Marquez, Y. Xia and G. V. Hartland, *J. Phys. Chem. C*, 2007, **111**, 12558–12565.
48 P. K. Jain, X. Huang, I. H. El-Sayed and M. A. El-Sayed, *Acc. Chem. Res.*, 2008, **41**, 1578–1586.
49 H. Wang, D. W. Brandl, F. Le, P. Nordlander and N. J. Halas, *Nano Lett.*, 2006, **6**, 827–832.
50 E. M. Larsson, J. Alegret, M. Käll and D. S. Sutherland, *Nano Lett.*, 2007, **7**, 1256–1263.
51 J. Rybczynski, U. Ebels and M. Giersig, *Colloids Surf., A*, 2003, **219**, 1–6.
52 W.-d. Ruan, Z.-c. Lu, N. Ji, C.-x. Wang, B. Zhao and J.-h. Zhang, *Chem. Res. Chin. Univ.*, 2007, **23**, 712–714.